Two-dimensional square and hexagonal oxide quasicrystal approximants in SrTiO 3 films grown on Pt(111)/Al 2 O 3 (0001)

Catalina Ruano Merchán, Thiago Trevizam Dorini, Florian Brix, Ludovic Pasquier, Maud Jullien, Danielle Pierre, Stéphane Andrieu, Karine Dumesnil, Sorour Semsari Parapari, Sašo Šturm, et al.

Two-dimensional square and hexagonal oxide quasicrystal approximants in $SrTiO_3$ films grown on $Pt(111)/Al_2O_3(0001)$

C. Ruano M.,[*,†,§] T. T. Dorini,[*,†,§] F. Brix ,[†,¶] L. Pasquier,[†] M. Jullien,[†] D. Pierre,[†] S. Andrieu,[†] K. Dumesnil,[†] S. S. Parapari,[‡,¶] S. Šturm,[‡,¶] J. Ledieu,[†,¶] M. Sicot,[†,¶] O. Copie,[†] E. Gaudry,[*,†,¶] and V. Fournée[*,†,¶]

†*Institut Jean Lamour UMR 7198, Université de Lorraine – CNRS, Nancy, France.*

‡*Jožef Stefan Institute, Jamova Cesta 39, Ljubljana 1000, Slovenia.*

¶*International Associated Laboratory PACS2, CNRS Université de Lorraine, Nancy, France and Jožef Stefan Institute, Ljubljana, Slovenia.*

§*Contributed equally to this work.*

E-mail: catalina.ruano-merchan@univ-lorraine.fr; thiago.trevizam-dorini@univ-lorraine.fr; emilie.gaudry@univ-lorraine.fr; vincent.fournee@univ-lorraine.fr

Abstract

The formation of two-dimensional oxide dodecagonal quasicrystals as well as related complex approximant phases were recently reported in thin films derived from $BaTiO_3$ or $SrTiO_3$ perovskites deposited on (111)-oriented Pt single crystal. Here, we use an all-thin-film approach in which the single crystal is replaced by a 10 nm thick Pt(111) buffer layer grown by molecular beam epitaxy on an $Al_2O_3(0001)$ substrate. An ultra-thin film of $SrTiO_3$ was subsequently deposited by pulsed laser deposition. The film stacking and structure are fully characterized by diffraction and microscopy techniques. We report the discovery of two new

complex phases obtained by reduction of this system through high temperature annealing under ultrahigh vacuum conditions. The formation of a new large square approximant with a lattice parameter equal 44.4 Å is evidenced by low-energy electron diffraction and scanning tunneling microscopy (STM). Additionally, a new 2D hexagonal approximant phase with a lattice parameter of 28 Å has been observed depending on the preparation conditions. Both phases can be described by two different tilings constructed with the same basic square, triangle and rhombus tiles possessing a common edge length of about 6.7 Å. Using the tiling built from high resolution STM images, we propose an atomic model for each approximant which accounts for the experimental observations. Indeed, the STM images simulated using these models are found in excellent agreement with the experimental ones, the bright protrusions being attributed to the topmost Sr atoms. In addition our theoretical approach shows that the adhesion of the oxide layer is rather strong (-0.30 eV/Å^2). This is attributed to charge transfer, from most electropositive elements (Sr and Ti) to most electronegative ones (Pt and O), and to hybridization with Pt-states. Density of states calculations indicate differences in the electronic structure of the two approximants, suggesting different chemical and physical properties. This all-thin-film approach may be useful to explore the formation of complex two-dimensional oxide phases in other metal-oxide combinations.

Introduction

Ternary oxides with perovskite structures ABO_3 have two cationic species (A, B) that can be selected among transition metals, simple metals, rare earths or even alkalis.[1–4] So many possible associations result in a large class of materials exhibiting various properties, from superconductivity to colossal magnetoresistance, from metal-insulator transitions to two dimensional (2D) electron gases.[1,3,4] When synthesized in the form of thin layers, new phenomena may appear related to the two dimensional nature of the structure.[5] In addition, when these ultrathin layers are supported on a metal, it becomes possible to more precisely control the stoichiometry of the films and their oxygen vacancy concentration compared to an all-oxide system, because interdiffusion phenom-

ena at the interfaces are largely suppressed.[5,6] The metallic substrate can also be used to modify the formation, structure and properties of the films, modifying the stress magnitude and the charge transfer at the interface. This is a rapidly growing field that has revealed the existence of new 2D oxide phases whose structures have no equivalent in bulk form.[5] These ultrathin reduced oxide layers are 2D materials that can be described most often from a few elementary tiles, such as MeO_4 squares (Me: a metal) or MeO_3 triangles. These tiles can be assembled together to pave the plane in different ways and form structures of various complexities. The understanding of the formation principles of such phases and the structure properties relationships are a subject of active research.

The report by Förster *et. al.* of a 2D oxide with a quasiperiodic structure and 12-fold rotational symmetry certainly represents the ultimate complexity in this material class.[7] Quasicrystals are long-range ordered materials that lack translational periodicity and exhibit classically forbidden rotational symmetries, like 5-, 8-, 10-, or 12-fold rotational symmetries.[8] They have been discovered in many intermetallic binary and ternary systems and also in soft matter. The report by Förster *et. al.* was the first example of a quasicrystalline oxide.[7] This 2D oxide quasicrystal (OQC) was obtained by reduction of a $BaTiO_3$ thin film grown on Pt(111). First, a few nanometer thick continuous $BaTiO_3$ film is grown by magnetron sputtering or by molecular beam epitaxy (MBE) on a Pt(111) single crystal substrate. Annealing the sample in an oxygen partial pressure at 900 K leads to a dewetting of the oxide film and the formation of isolated $BaTiO_3$ 3D islands on the bare Pt(111). A subsequent annealing at 1020 K under ultrahigh vacuum (UHV) leads to a re-wetting of the surface where a 2D layer coming from the edges of the islands covers the entire Pt(111) surface. When annealing at higher temperatures (above 1170 K), a 2D OQC structure develops between the oxide islands. The process is reversible, meaning that the 2D quasicrystalline film decays when annealed again in an oxygen partial pressure at 900 K, transforming back into isolated crystalline $BaTiO_3$ islands on the bare Pt (111) substrate.[9]

The quasiperiodic nature of this oxide thin film was evidenced by low-energy electron diffraction (LEED) pattern exhibiting 12-fold rotational symmetry and by high-resolution scanning tun-

neling microscopy (STM) images showing bright protrusions located at the node of the so-called Niizeki-Gähler tiling (NGT tiling), the archetype dodecagonal tiling.[10] This tiling paves the plan with three different tiling elements - equilateral triangles, squares and 30° rhombuses - appearing in specific ratio 2.73: 1: 0.37 (the number of triangles relative to the number of squares and of rhombuses). Later, Schenk *et al.* also reported the formation of a similar OQC at the interface of a $SrTiO_3$ (STO) thin film grown on the same (111)-oriented Pt substrate,[11] suggesting that OQC formation could be extended to different metal-oxide combinations.

Besides formation of quasiperiodic phases, related periodic phases presenting similar atomic arrangements on a local scale were observed.[11,12] These structures are called approximants and can be described from the same tiling elements as for the quasicrystal but with different tiling element ratio. Approximant phases can exhibit physical properties similar to those of the parent quasicrystal with the advantage that they may be easier to study theoretically, since all of the methods established for periodic crystals may be applied to them.[13] In the STO/Pt(111) system, only one approximant has been reported, with an oblique unit cell formed by 36 tiling elements.[11]

The vast configurational space generated by the numerous combinations of perovskites and metal support is expected to lead to a wide range of attractive properties, as it has recently been demonstrated in the case of the sigma-phase.[14] However, the number of ABO_3/Me(111) couples experimentally investigated so far is still very limited. Here, we report an all-thin-film approach to investigate ABO_3/Me(111) systems in a more versatile and less expensive way than using single crystal metal substrates. We investigate this possibility by growing a Pt(111) buffer layer on Al_2O_3(0001) substrate by MBE, on which we grow $SrTiO_3$ thin film by pulsed laser deposition (PLD). The thin film stacking architecture is presented in a schematic in Fig1 (a). By using STM and LEED, we identify two new approximant phases, one with a giant square-like unit cell and another with a large hexagonal structure, both obtained after oxidation-reduction cycles of the thin film stacking. Both phases are described from the same tiling elements than the previously

observed OQC and monoclinic approximant, but assembled in different ways. Using the tiling decoration proposed by Cockayne *et al.*,[15] a structure model is constructed for both phases. Simulated STM images based on density functional theory (DFT) calculations are found in excellent agreement with the experimental data. Contrary to the literature,[16] the results indicate that the STM contrast mainly originates from Sr atoms slightly protruding above the mean surface plane. Total energy calculations show that the adhesion of the oxide layers are similar for the square and hexagonal complex structures, attributed in both cases to electronic interactions - charge transfer and hybridization - between the adlayer and the substrate. This is consistent with the trends between the adhesion energies and electronic factors, already identified for other types of oxide adlayers on metal substrates.[14,17]

Experimental and theoretical details

Sample fabrication

The sample fabrication was performed in two different UHV chambers interconnected by an UHV tube, both chambers being equipped with a reflection high energy electron diffraction (RHEED) setup. First, 10 nm of Pt were grown by molecular beam epitaxy (MBE) on a Al_2O_3(0001) substrate (SurfaceNet GmbH) previously degassed at 1173 K in UHV for 15 minutes. The Pt growth was performed at a substrate temperature of 673 K (pressure $< 10^{-9}$ mbar). Then, 0.8 nm of STO were deposited by PLD on the Pt buffer layer using a KrF excimer laser (248 nm) at 1 Hz pulse repetition and a fluence of 0.4 J/cm^2. XRD characterizations were performed with a MRD X'Pert Pro diffractometer in a Bragg-Brentano configuration, using Cu K_α radiation ($\lambda = 1.54056$ Å).

Another sample was used to analyze the film in cross-section by transmission electron microscopy (TEM). For that purpose, a 10 nm thick STO film was grown on a 10 nm Pt buffer layer deposited on Al_2O_3(0001) substrate. The Pt buffer layer was enriched with a 1 nm thick Ti layer followed by an annealing at 1073 K to promote intermixing. According to the literature, it facilitates the epitaxial growth of STO with (111) orientation on Pt.[18] However, all phases reported

here were observed independently of the presence or not of this Ti layer and had no observable effects. An electron-transparent lamella was prepared in a cross-sectional view by a focused ion beam scanning electron microscope (FIB-SEM; Helios NanoLab 600i dual beam system, Thermo Fisher Scientific, previously FEI company, Eindhoven, The Netherlands). Prior to the lamella preparation, a 30 nm thick carbon layer was deposited on the sample in order to protect the surface layer during the FIB lamella preparation. The experimental high-angle annular dark-field scanning transmission electron microscopy (HAADF-STEM) images were recorded, to directly assess the atomic structure and orientation relationship, using a probe Cs-aberration-corrected TEM (JEM-ARM 200CF; JEOL, Tokyo, Japan) operated at 200 keV, with a spatial resolution in STEM mode of 0.08 nm. The atomically-resolved STEM images were processed using an Average Background Subtraction Filter (ABSF)[19] to reduce the contributions from amorphous phases. The collection semi-angle for the HAADF detector was set between 68–280 mrad.

Surface characterization

The STO films are stable under ambient conditions, which allowed sample transfer through air to a different UHV system in which oxidation and reduction cycles were performed followed by *in situ* surface characterizations using low energy electron diffraction (LEED), room temperature scanning tunneling microscopy (STM) and x-ray photoemision spectroscopy (XPS).

After re-entering the samples in UHV, an annealing in 1×10^{-6} mbar of O_2 at 900 K was performed to remove surface contamination induced by the transfer as confirmed by XPS. The reduction step consists in further annealing of the film stacking to higher temperatures (> 1123 K) and under UHV conditions ($< 10^{-8}$ mbar). The temperature was monitored with a pyrometer with the emissivity set to 0.8. STM images were processed with the WSxM software.[20]

Computational details

All calculations were performed with Density Functional Theory (DFT) using the Vienna *ab initio* simulation package (VASP)[21–23] combined with the Atomic Simulation Environment (ASE).[24]

Spin-polarised calculations were performed with plane-wave basis set and projector-augmented wave (PAW) method,[25,26] using the optPBE functional.[27,28] The following electrons were treated explicitly: $4s^2 5p^6 6s^2$ (Sr), $2s^2 2p^4$ (O), $3s^2 3p^6 4s^2 3d^4$ (Ti), $5d^9 6s^1$ (Pt). The strong on-site Coulomb interaction of localized electrons was treated through the GGA+U approach,[29] using U(Ti) = 1.0 eV.[30,31] This value has been chosen because it provides a good agreement with theoretical quantities calculated using the hybrid HSE03 exchange correlation potential, as demonstrated recently in the case of an oxide layer with the honeycomb structure supported on a metal substrate.[30,32] The one-electron Kohn-Sham orbitals were expanded in a plane-wave basis set with a kinetic energy cutoff of 500 eV. Total energies were minimised until the energy differences were less than 10^{-5} eV between two electronic cycles. The reciprocal space integration was sampled at the Γ-point for total energy calculations. The partial occupancies have been considered within the Methfessel-Paxton scheme with a smearing equal to 0.2 eV. A thinner k-point grid ($2\times2\times1$) was used for the DOS (Density of States) calculations for the hexagonal structure (surface cell 28.20 Å $\times$ 28.20 Å). This set-up gives cohesive energies and lattice parameters of bulk systems in good agreement with the experimental data.[14]

The ultrathin oxide (UTO) films supported on Pt(111) have been built using 4-layer thick asymmetric slabs consisting of three Pt(111) layers and one oxide-layer. The outmost bottom layer of the Pt substrate was kept fixed, while all other layers were allowed to fully relax in all directions, using the Conjugate Gradient Algorithm, until all forces were less than 0.1 eV/Å. Adjacent slabs (along the surface normal direction) were separated by a 15 Å thick vacuum layer and a dipole correction was applied to cancel the artificial electric field that develops due to imposed periodic boundary conditions in surface normal direction. The average charges on each atom were calculated using the Bader approach,[33] using the code distributed by the Henkelman group.[34–37] The STM images were calculated using the Tersoff-Hamman approximation.[38,39] Charge deformations were calculated by the difference $\rho_{UTO/Pt} - \rho_{Pt} - \rho_{UTO}$, where $\rho_{UTO/Pt}$, ρ_{Pt} and ρ_{UTO} are the charge densities of the UTO/Pt(111) slab, Pt(111) slab and UTO free standing layer, respectively. Structures and STM images were plotted using the VESTA and p4vasp softwares, respectively.[40]

The formation enthalpies are given by

$$\Delta H_{\mathrm{f}} = E(\mathrm{Pt_wSr_xTi_yO_z}) - wE_{\mathrm{coh}}(\mathrm{Pt}) - xE_{\mathrm{coh}}(\mathrm{Sr}) - yE_{\mathrm{coh}}(\mathrm{Ti}) - \frac{z}{2}\mu_{\mathrm{O_2}} \quad (1)$$

where E and E_{coh} are total and cohesive energies, respectively and $\mu_{\mathrm{O_2}}$ is the chemical potential of dioxygen. Adhesion energies are calculated using

$$E_{\mathrm{adh}} = E(\mathrm{UTO/Pt}) - E(\mathrm{UTO}) - E(\mathrm{Pt}) \quad (2)$$

where $E(\mathrm{UTO/Pt})$, $E(\mathrm{UTO})$ and $E(\mathrm{Pt})$ are the total energies of the supported UTOs, the ideal freestanding UTOs and the Pt(111) substrate, respectively. A single point calculation, without any geometry optimization, has been performed to evaluate E(UTO) and E(Pt).

Results and discussion

Thin films stacking

The film structure was probed *in situ* at the different stages of the sample fabrication by RHEED. Fig.1 (b) presents the RHEED patterns along the $[11\bar{2}0]_{\mathrm{Al_2O_3}}$ and $[10\bar{1}0]_{\mathrm{Al_2O_3}}$ directions, starting with the diffraction pattern of the clean substrate. After Pt deposition at 673 K, the RHEED pattern exhibits sharp elongated streaks repeated every 60° confirming a 6-fold surface symmetry of the epitaxial thin film. Blue arrows indicate the matching of the streaks after the film deposition. The next RHEED patterns are obtained after growing the STO film on the Pt buffer layer at 1073 K. The spotty pattern indicates that the STO ultra thin film is (111)-oriented with the presence of surface islands when grown on the Pt(111) surface.

A high resolution X-ray diffraction (HRXRD) $\omega - 2\theta$ measurement of the Pt film grown on Al_2O_3 (0001) substrate is shown in Figure 1(c). The substrate reflections are clearly observed along

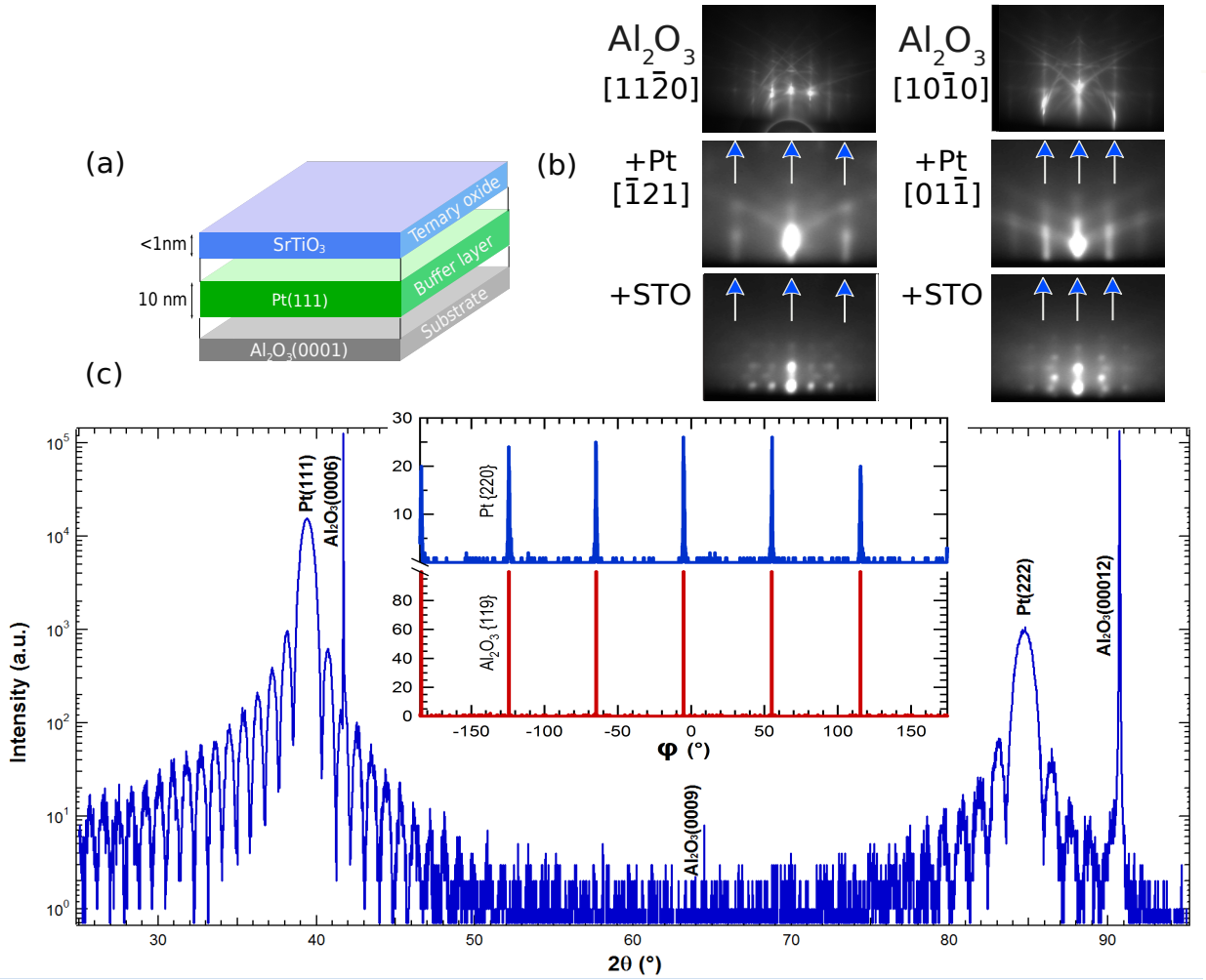

Figure 1: (a) Sample architecture consisting in a thin film stacking configuration. (b) RHEED patterns: before film growth; after deposition of 10 nm of Pt; after deposition of 0.8 nm of STO. (c) HRXRD $\omega - 2\theta$ scan of the Pt buffer layer growth on an $Al_2O_3(0001)$ substrate and the XRD φ-scans along the reflection planes $\{220\}$ and $\{119\}$ of the Pt film and the substrate respectively.

with the *hhh* reflections of the Pt. No reflections from other planes are present indicating that Pt is well (111)-oriented. Laue oscillations on both sides of the Pt(111) and Pt(222) reflection peaks suggest good crystallinity and high interface quality. Figure 1(c) also shows the φ-scan of the Pt film and substrate measured using the reflection planes $\{220\}$ and $\{119\}$ respectively. Six peaks separated by 60° for both, substrate and film, are evidence of the six-fold symmetry and moreover the epitaxial growth of Pt(111) on the $Al_2O_3(0001)$ substrate. These RHEED and HRXRD results confirm the epitaxial relationships:

$(111)_{Pt} \parallel (0001)_{Al_2O_3}$; $[01\bar{1}]_{Pt} \parallel [10\bar{1}0]_{Al_2O_3}$ and $(111)_{SrTiO_3} \parallel (111)_{Pt}$.

Figure 2(a) shows an HAADF-STEM image of the thicker sample previously mentioned. The FIB lamella was cut perpendicular to the $[10\bar{1}0]_{Al_2O_3}$ direction. The measured thickness of the buffer layer is about 12 nm and that of the $SrTiO_3$ film is 10 nm, in agreement with expected values. The interfaces at both Pt/Al_2O_3 and $Pt/SrTiO_3$ are relatively sharp. Due to the slight thickness difference of the projected layers along the viewing direction and the resulting variation in corresponding focal planes, the atomic structure of each layer could not be observed simultaneously in one image. Instead, atomically resolved ABSF-filtered HAADF-STEM images are shown at their corresponding zone axes $[10\bar{1}0]_{Al_2O_3}$, $[110]_{Pt}$ and $[110]_{SrTiO_3}$ respectively. Various crystalline grains are present in the $SrTiO_3$ layer, corresponding to different variants,[18] whose average grain size lies at around 15 nm.

For determining the orientation relationship between the Pt and STO layers and inspecting the interface quality, the STEM imaging was carried out at the interfacial region with atomic resolution. Fig 2(b) presents an HAADF-STEM image of the Pt/STO interfacial region. The Pt and STO layers are viewed along the $[110]_{Pt}$ and $[110]_{SrTiO_3}$ zone axes, respectively. The corresponding superimposed structural models of Pt and STO are in good agreement with the underlying atomic-resolution STEM image. The atomically-sharp interface is present between the Pt layer and the STO thin film. The fast-Fourier transform (FFT) pattern calculated from the dotted marked region on the HAADF-STEM image is shown in Fig 2(c). Some of the spots on the FFT pattern are assigned to the Pt and STO atomic planes. The analysis confirms that the (111)Pt lattice planes are parallel to (111)STO planes. The orientation relationship deduced from the FFT pattern is $(111)_{Pt}[110]_{Pt} \parallel (111)_{SrTiO_3}[110]_{SrTiO_3}$.

Experimental investigation of the $SrTiO_3$-derived square approximant

Figure 3 (a) shows the LEED pattern of the surface of the STO(0.8 nm)/Pt(10nm)/Al_2O_3(0001) sample after degassing to remove air contamination. At 50 eV the diffraction pattern reveals a well (111)-oriented STO film (diffraction spots marked in orange) epitaxially grown on the Pt(111)

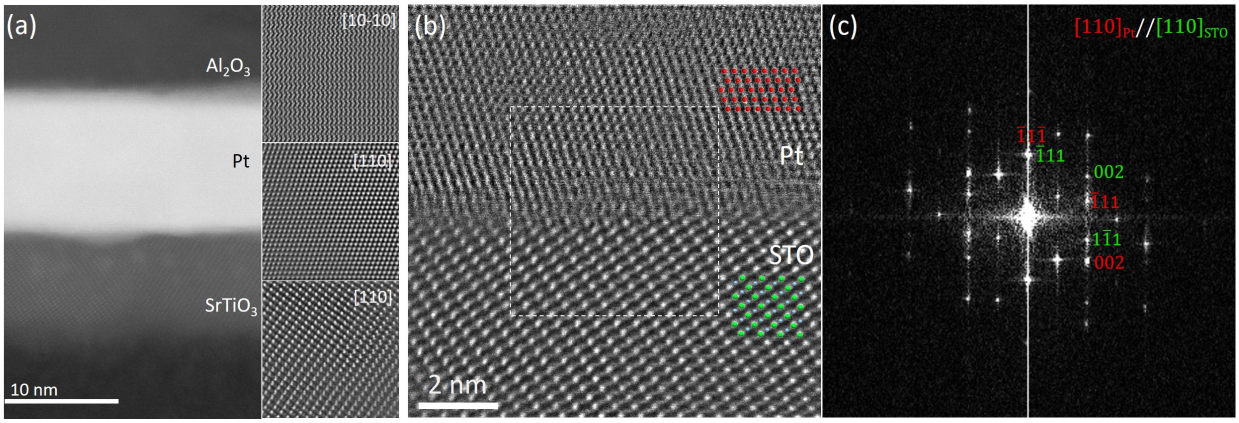

Figure 2: (a) HAADF-STEM image showing the thin film stacking, consisting of Al_2O_3 substrate, $\sim$ 12 nm Pt buffer layer and $\sim$ 10 nm $SrTiO_3$ thin film. The atomically-resolved HAADF-STEM images of each layer are shown on the right at their corresponding zone axes of $[210]_{Al_2O_3}$, $[110]_{Pt}$ and $[110]_{STO}$, respectively. (b) Atomically resolved ABSF-filtered HAADF-STEM image of the Pt/STO interfacial region with the superimposed structural models viewed in the $[110]_{Pt}$ and $[110]_{STO}$ zone axes, respectively. Pt, Sr and Ti atoms are shown in red, green and blue, respectively. (c) The corresponding FFT pattern obtained from the marked area in (b).

buffer layer (diffraction spots marked in blue). The surface lattice parameter of STO is twice as large as that of the Pt(111). Then, by annealing the surface at higher temperatures (> 1123 K) in UHV (< 10^{-8} mbar) a new structure with an apparent dodecagonal symmetry was formed as observed by LEED and STM. This is illustrated in the LEED pattern at 20 eV with 12 intense diffraction spots as can be seen in Figure 3 (b). At higher beam energies (see Fig.3 (c)), higher order diffraction spots are observed leading to a LEED pattern very similar to the one reported previously for the OQC.[11] The 6-fold diffraction spots from the Pt buffer layer are marked by the blue circles.

The real space structure and the local atomic arrangements were determined from atomically resolved STM images taken at room temperature (figure 4 (a)). Although the LEED pattern shows an apparent dodecagonal pattern typical of an OQC, the fast Fourier transform (FFT) of the real space image reveals a periodical almost square lattice, indicating that an approximant was formed instead of an OQC.[41–44] The FFT was used to determine the lattice parameters. Figure 4 (b) gives a more detailed view of the identified approximant unit cell, with the in-plane measured lattice parameters of: 42.2$\pm$ 0.6 Å$\times$ 43.2 $\pm$ 0.6 Å, and angle between edges of 89.7 $\pm$ 0.4°. The

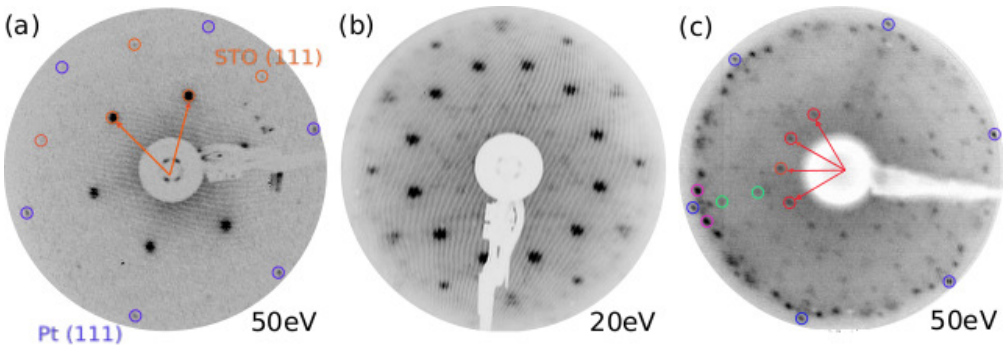

Figure 3: (a) LEED pattern of the STO thin film deposited on 10 nm of Pt(111). First order diffraction spots of the oxide are marked in orange. Pt buffer layer first order diffraction spots are highlighted in blue. (b) LEED pattern of the square approximant formed on Pt(111) at 20 eV and (c) at 50 eV. Some of the spots in the outer ring appear as triplets in (b). The blue circles mark the Pt(111) first order diffraction pattern. Higher order diffraction spots of the approximant are marked in red, green and magenta circles.

bright protrusions seen in the STM images are at the nodes of the same Stampfli–Gähler tiling elements used to describe dodecagonal structures.[10] These tiling elements are arranged such that the unit cell contains 72 tiles, namely 48 triangles, 18 squares and 6 rhombus with a tiling element ratio of 2.66:1:0.33. This is twice the number of tiles needed to describe the previously reported monoclinic approximant,[11] but the ratio remains the same. Besides, it is just slightly different from the ideal NGT structure of the dodecagonal QC phase given by 2.73:1:0.37. The unit cell contains 47 vertex atoms, corresponding to an area density of 2.20 nm^{-2}, smaller than the values reported for the OQC phase (2.46 nm^{-2}). From the STM image, an average distance of 6.4 $\pm$ 0.3 Å between the bright protrusions is deduced. The edge length of the tiling elements deduced from the ideal unit cell is 42.2 Å/(3 + 2 $\sqrt{3}$) = 6.53 Å, for the vertical axis, and 43.2 Å/(3 + 2 $\sqrt{3}$) = 6.68 Å, for the horizontal axis. One axis of the approximant unit cell is parallel to the [12$\bar{3}$] direction of the hexagonal Pt buffer layer. From the idealized unit cell model, it is possible to obtain a FT of the structure, as shown in the left side of Fig.4 (c) where the near 12-fold first order, second order and third order diffraction spots are present as part of a square lattice indicated in green. The calculated FT pattern perfectly matches the FFT of the experimental STM image (right side 4 (c)). The tiling decoration is shown in Figure 4 (d).

The unit cell of the approximant can be expressed as a superstructure with respect to the Pt(111)

lattice, resulting in a commensurate matrix given by $\begin{pmatrix} 16 & 0 \\ 9 & 18 \end{pmatrix}$ when the dimensions of the unit cell are slightly modified to 44.87 Å$\times$ 43.75 Å, with an angle between edges of 89.7° and the Pt(111) unit cell is fixed to 2.79 Å. Six rotational domains of the approximant, with three unique subpatterns, exist from the square-like structure on the hexagonal lattice of the Pt(111) buffer layer. As a result, some of the diffraction spots in the LEED pattern are split into three reflexes as can be seen at low primary beam energies (Fig. 3(b)). The square lattice is not clearly visible in the diffraction pattern (Fig. 3), probably due to the fact that many of the diffraction spots may have a weak intensity and the LEED patterns are dominated by the most intense spots.

Experimental investigation of the $SrTiO_3$ derived hexagonal approximant

With increasing numbers of oxidation-reduction cycles under the same experimental conditions as described earlier, another new UTO phase was observed with a large hexagonal unit cell. Figure 5 (a) and (b) show high resolution STM images of this structure, as well as the tiling decoration. The FT calculated from this tiling decoration as well as the FFT calculated from the experimental STM image are shown in Fig. 5 (c). It is also possible to observe more intense higher-order spots in the calculated FT which form a pseudododecagonal ring which is included in the hexagonal lattice. It reflects the presence of local dodecagonal motifs. The dimensions of the unit cell are 27.8 $\pm$ 0.6 Å$\times$ 28.1 $\pm$ 0.6 Å. This hexagonal unit cell can be decorated with the same Stampfli–Gähler tiling elements. It contains 29 tiles, namely 20 triangles, 6 squares and 3 rhombus as shown in Fig.5(c). A common edge length of 6.7 $\pm$ 0.2 Å is deduced from the average distance between the bright protrusions. Dodecagonal rings consisting of 6 squares and 12 triangles decorate the node of the unit cell. A protrusion is usually missing at each node of the hexagonal unit cell (ie. at the center of the dodecagonal rings) in the images shown in Fig. 5(a) and (b). In other patches of the surface, this site is occupied and appears as a bright dot, suggesting the presence of slightly protruding atoms. STM images of the two variants of the hexagonal approximant are shown in the supplementary material (Fig. S1). The unit cell contains either 19 or 18 vertex, corresponding

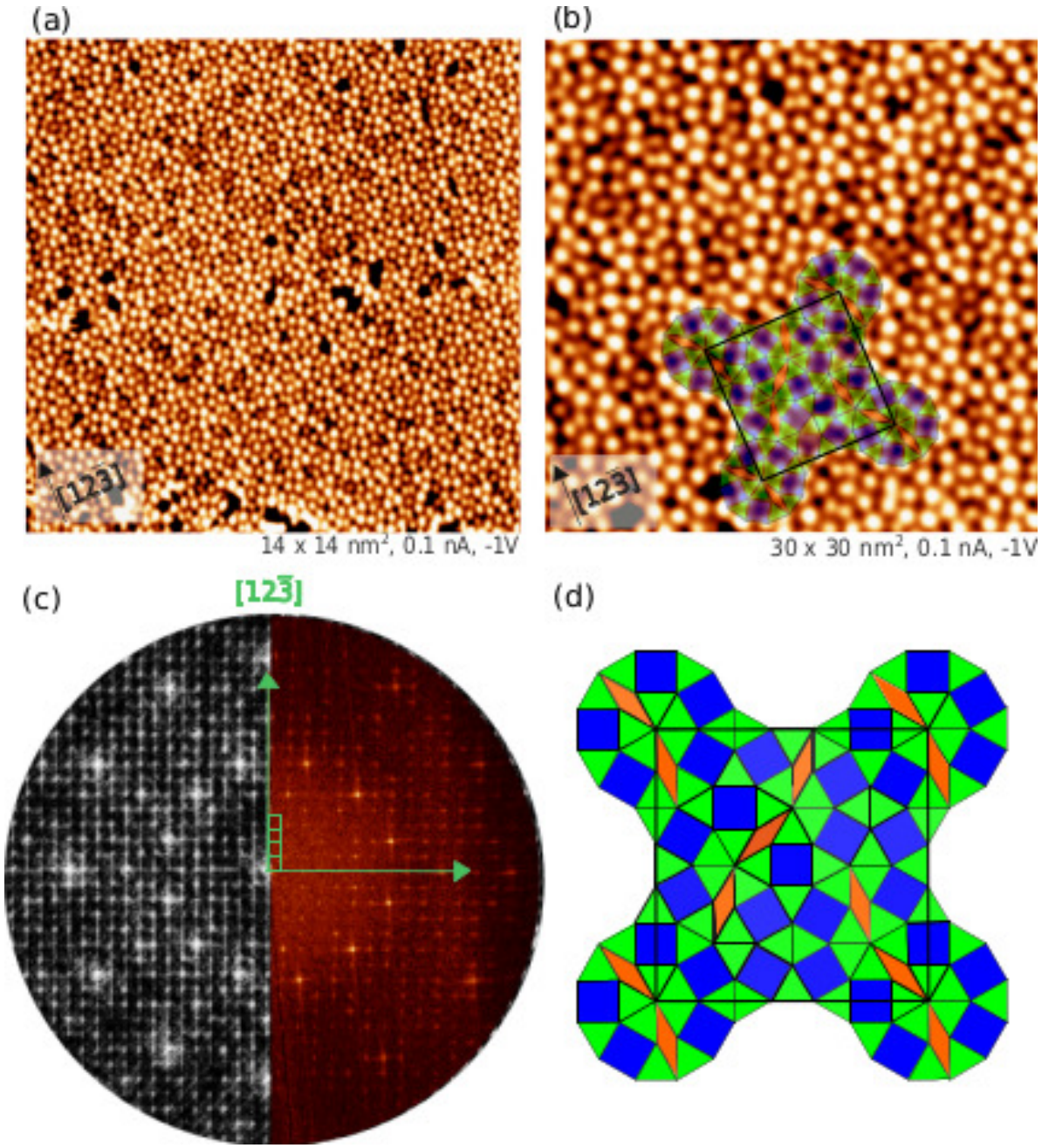

Figure 4: (a) Atomically resolved STM image of the STO derived approximant formed on Pt(111). (b) STM image of the square approximant with the square-like unit cell superimposed. (c) Left: calculated FT of the idealized tiling. Right: FFT of the STM image in (a). The square unit cell is marked in green with one of the axes oriented in the $[12\bar{3}]$ direction of the Pt(111) buffer layer. (d) Tiling decoration of the square unit cell.

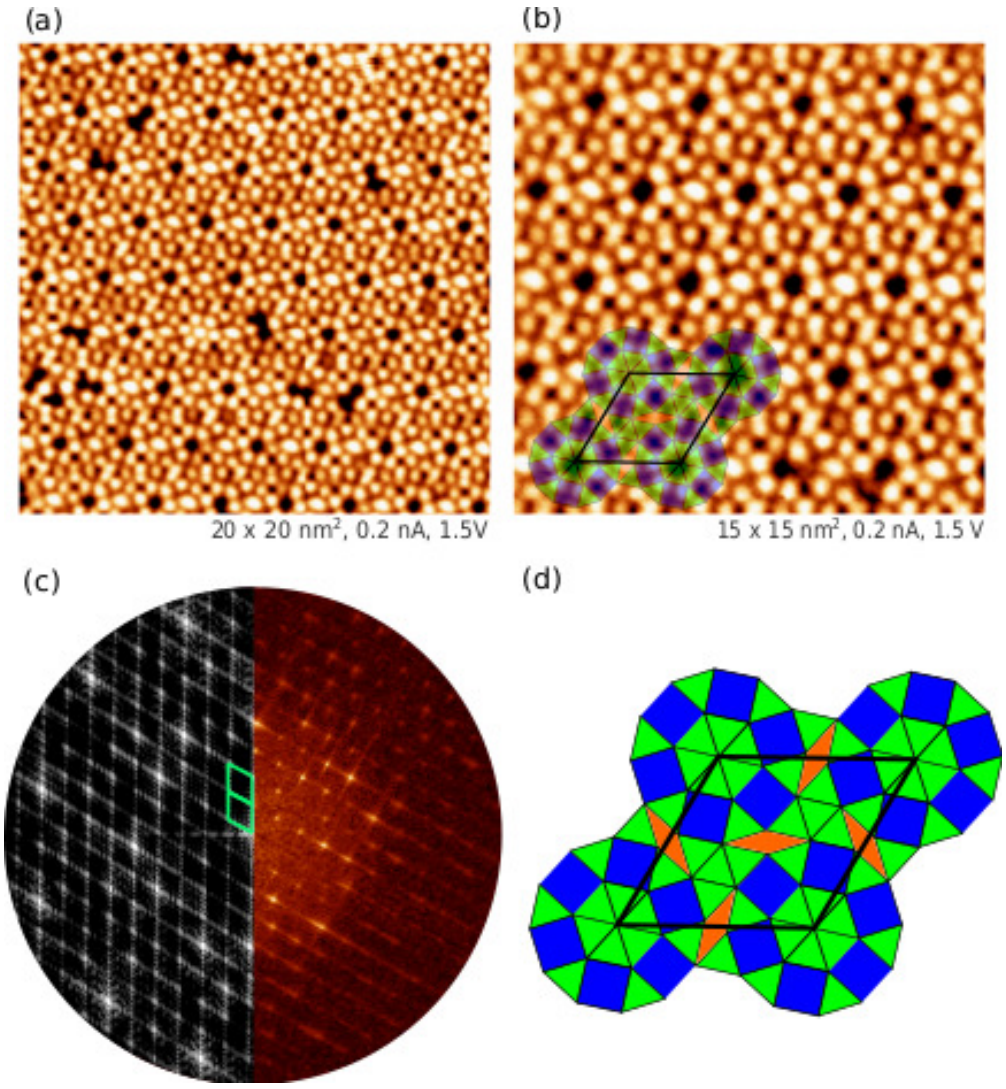

Figure 5: (a) Atomically resolved STM image of the STO derived large hexagonal phase formed on Pt(111). (b) Idealized unit cell of the large hexagonal phase decorated by the dodecagonal tiling elements: squares, triangles and rhombuses superimposed on the real STM image. (c) Left: calculated FT of the idealized tiling. Right: FFT of the STM image in (a). The hexagonal unit cell is marked in green. (d) Tiling decoration of the hexagonal unit cell.

to an area density between 2.65 and 2.80 nm^{-2}, significantly larger than that of the ideal OQC or its square approximant. The tiling elements ratios of the hexagonal phase is 3.33:1:0.5, which differ considerably from the ideal OQC or the square approximant. The structural evolution of the UTO film, from square-like to hexagonal approximant , could be related to a change in the stoichiometry with the number of annealing cycles. The LEED pattern of the hexagonal phase is shown in Fig. 6. Four non-equivalent domains can be identified, which are rotated with respect

to the $[1\bar{1}0]_{Pt}$ direction by 15°, 27°, 34° and 45°. We tentatively ascribed these domains to the following four commensurate structures with matrices given by $\begin{pmatrix} 6 & -5 \\ 5 & 11 \end{pmatrix}$ and $\begin{pmatrix} 5 & -6 \\ 6 & 11 \end{pmatrix}$ for the domains presented in green in Fig.6, when the lattice parameter of the hexagonal phase is 26.61 Å and the Pt(111) unit cell is fixed to 2.79 Å and $\begin{pmatrix} 8 & -3 \\ 3 & 11 \end{pmatrix}$ and $\begin{pmatrix} 3 & -8 \\ 8 & 11 \end{pmatrix}$ for the domains marked in pink in Fig. 6 when the lattice parameter of the hexagonal phase is 27.48 Å and the Pt(111) unit cell is fixed to 2.79 Å.

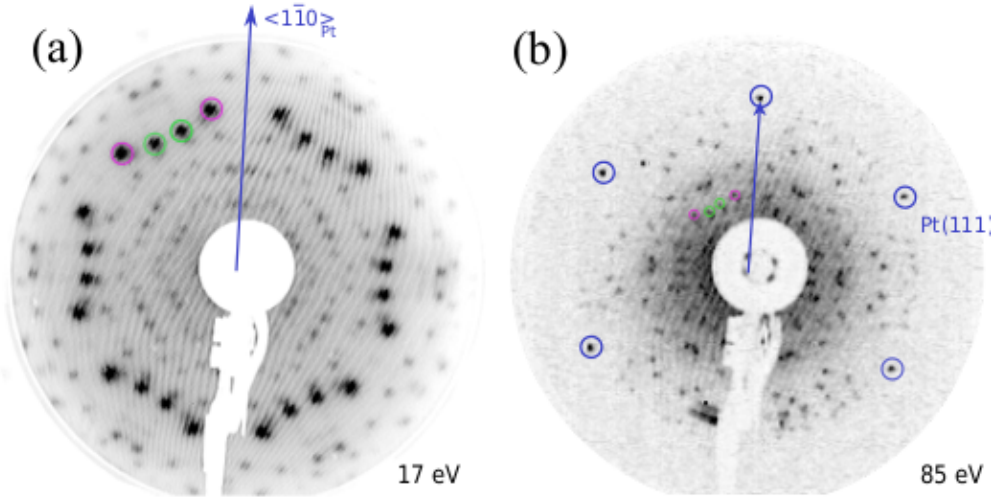

Figure 6: LEED patterns of the large hexagonal phase of STO/Pt(111). (a) At 17 eV, four non-equivalent domains are identified. The domains are rotated by 15°, 27°, 34° and 45° with respect to the $[1\bar{1}0]_{Pt}$ direction. (b) At 85 eV, Pt buffer layer first order diffraction spots are evident. These are highlighted in blue.

Theoretical investigation of the two 2D complex oxide phases

The structural and electronic properties of the square and hexagonal approximants are investigated using two model structures based on the complex tilings identified above (Figs. 7-8). They are made of structural motifs – equilateral triangles, squares and 30^o rhombuses – sharing a common side length. The atomic structure of each type of tiles has been implemented using the models proposed by Cockayne *et al.* for $BaTiO_3$ and replacing Ba by Sr atoms.[15] Thus, the chemical compositions of the triangles, squares and rhombuses are $SrTiO_3$, $SrTi_4O_4$ and $SrTi_2O_2$, respec-

tively. The Sr atoms are located at the vertices of the tiling. Each Ti atom is bound to three oxygen atoms (local 3-fold symmetry), and each oxygen atom is located between two Ti atoms. The square and rhombus motifs share common sides with the triangular tiles, while the square and rhombus motifs are connected through the vertices. This atomic arrangement is quite different from the $3^2.4.3.4$ Archimedean tiling (σ-phase) identified by Förster *et al.*,[12] where Ti atoms are located at the vertices of the square and triangle tiles. It is also quite different from the honeycomb structure, that consists of a Ti_2O_3 single-layer doped with alkali earth atoms, as experimentally observed for Ti_2O_3/Au(111).[45] With this tile decoration model, the chemical composition of the square approximant is $Sr_{0.36}TiO_{1.54}$ and that of the hexagonal phase is $Sr_{0.38}TiO_{1.56}$. These are very close to that of the ideal NGT tiling of the quasicrystalline phase with the same tile decoration model which is $Sr_{0.37}TiO_{1.55}$.[15] The surface atom densities of the square approximant and the hexagonal phase are 19.56 and 18.7 atom.nm^{-2} respectively. The number of Sr atoms per surface unit cell deduced from these values are in agreement with the number of vertices per unit cell deduced from the experimental STM images.

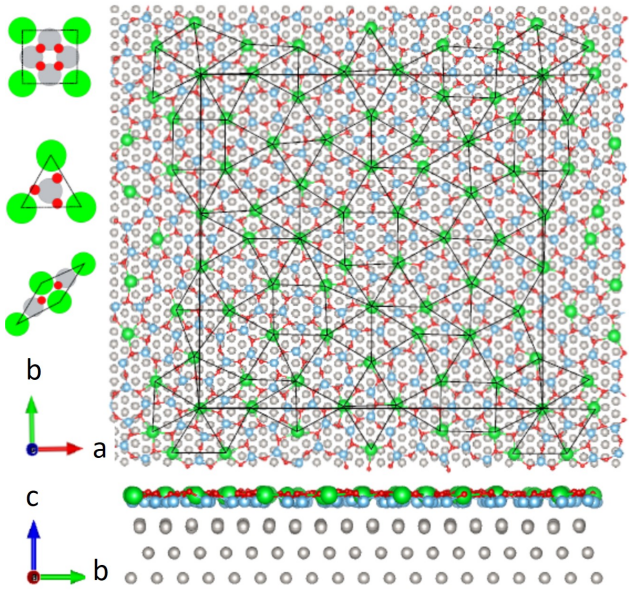

Figure 7: Top and side views of the relaxed approximant structure, along with the three types of tiles used to build it. Sr, Ti, O and Pt atoms are shown in green, blue, red and silver respectively.

The two complex UTOs present similar formation enthalpies: -1.03 eV/Å^2 and -1.08 eV/Å^2 for

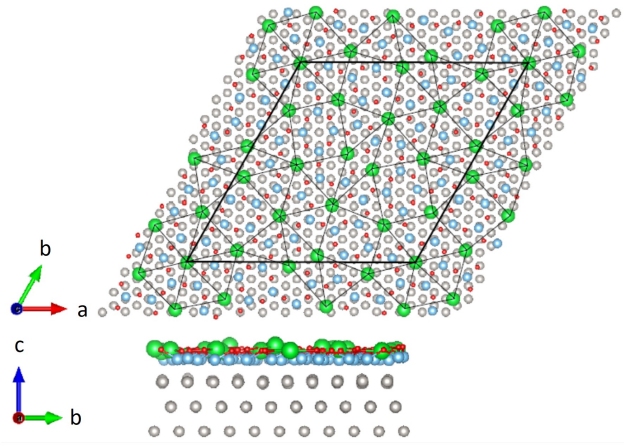

Figure 8: Top and side views of the relaxed complex hexagonal structure. Sr, Ti, O and Pt atoms are shown in green, blue, red and silver respectively.

the square and hexagonal phase respectively. They also present similar adhesion energies (-0.28 eV/Å^2 and -0.30 eV/Å^2 for the square and hexagonal phase respectively). They are much stronger than the one calculated for the σ-phase (-0.11 eV/Å^2), likely because the atomic surface density is larger for the complex UTOs than for the σ-phase. They are weaker than the one calculated for the honeycomb structure (-0.42 eV/Å^2). It suggests that the presence of common symmetries between the substrate and the adlayer lead to a stronger interaction.

When supported on Pt(111), UTOs display significant structural relaxations in the z direction, i.e. the surface normal direction. Such corrugation can alleviate the elastic strain due to the size-mismatch between the unsupported and supported films.[14,30] It is quantified by the vertical separation between the average z-position of the anions (z^-) and cations (z^+). The rumpling $R = z^+ - z^-$ is negative for the two complex systems (Tab. 1). Indeed, the mean vertical distance between the topmost Pt atoms and the Ti atoms is much smaller (2.3 Å) than the one between topmost Pt atoms and the oxygen or strontium atoms (3.1 Å and 3.2 Å, respectively), in agreement with the values obtained by Cockayne *et al.* for $BaTiO_3$.[15] The rumpling is found much larger for the complex UTOs ($R^{\text{approx}} = -0.41$ Å and $R^{\text{hex}} = -0.47$ Å for the approximant and hexagonal structures, respectively) than for the UTOs with a smaller surface cell ($R^{\sigma} = -0.22$ Å and $R^{\text{honeycomb}} = -0.26$ for the σ-phase and the honeycomb structure, respectively).

These structural results can be rationalized by a Bader charge analysis. Charge transfer is found

to occur at the Pt-UTO interface, from most electropositive elements (Sr, Ti) to most electronegative elements (Pt and O). Thus, electrostatic interactions likely contributes to the location of Ti cations close to the negatively charged Pt substrate, while repelling the negative O atoms.[15] This is further confirmed by the charge density deformation, which indicates non negligible charge differences at the Pt-UTO interface. More generally, electronic effects are known to impact the rumpling and the adhesion energies. Using the σ-phase, a correlation has been evidenced between the Bader charge carried by the transition metal atoms (Q_{TM}) and both R and E_{adh}. Overall, a larger Q_{TM} leads to a stronger adhesion of the film and a larger R.[14] The same trends are observed in this work. Indeed, the Bader charges of Ti atoms are calculated to be larger in the approximant and hexagonal complex UTO structures (2.04 e and 2.07 e, respectively) than in the σ and honeycomb UTOs (1.99 e), in agreement with a larger R and E_{adh}.

Table 1: Bader charges on ions, as well as the rumpling and the adhesion energies.

	Approximant	Hexagonal	σ phase	Honeycomb
	Freestanding UTO			
Q_{Ti} (e)	1.46	1.40	1.90	1.47
Q_{Sr} (e)	1.51	1.51	1.60	1.51
Q_{O} (e)	−1.29	−1.27	−1.30	−1.22
	Supported UTO			
R(Å)	−0.41	−0.47	−0.22	−0.26
Q_{Ti} (e)	2.04	2.07	1.99	1.99
Q_{Sr} (e)	1.48	1.41	1.56	1.61
Q_{Pt} (e)	−0.11	−0.11	−0.10	−0.08
Q_{O} (e)	−1.22	−1.17	−1.10	−1.13
E_{adh} (eV/Å^2)	−0.28	−0.30	−0.11	−0.42
ΔH_f (eV/at)	−1.03	−1.08	−0.42	−1.52

For each complex UTO, the STM images are simulated for both positive and negative biases (Figs.9-10, Fig. S2). The bright contrast is attributed to the protruding Sr atoms, while the Ti and O atoms are not visible, in agreement with the average z-positions of Sr, Ti and O described previously. Overall, the good agreement between the simulated and experimental STM images (Figs. 4-5) suggest that the UTO structural models considered in this work are realistic models for

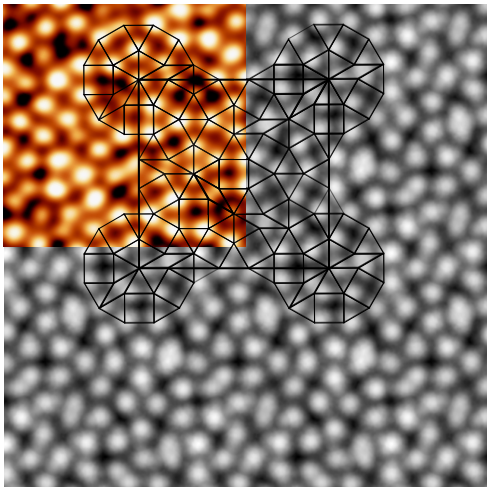

Figure 9: Simulated STM image of the square approximant ($V_{bias} = -1$ V, isosurface with charge density equal to 0.1 e nm^{-3}). A fraction of the experimental STM image (Fig.4) is shown in the upper left corner.

the new complex UTOs synthesized here and has been further confirmed by recent surface x-ray diffraction experiments.[46]

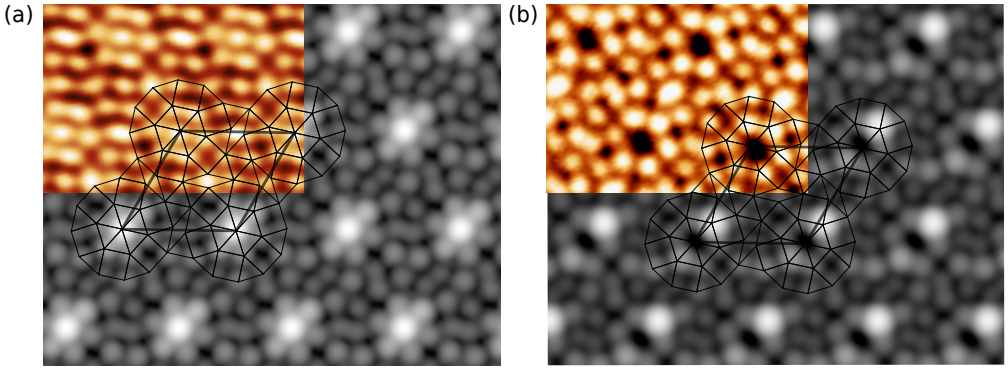

Figure 10: Simulated STM images of the complex hexagonal phase. The two variants have been considered, either with (a) or without (b) the central protrusion at the center of the dodecagonal motifs. The STM images have been calculated at the same bias as the experimental ones, shown in the upper left corner of each panel. ((a) $V_{bias} = -1$ V, isosurface with charge density equal to 0.2 e nm^{-3}, (b) $V_{bias} = +1.5$ V, isosurface with charge density equal to 0.1 e nm^{-3}).

Density of states calculations have been performed using the two complex UTO structures (Fig. 11). In both cases, the contribution of Sr atoms to the DOS is weak below the Fermi level, thus corroborating the Bader analysis. The main contribution to the DOS at the Fermi level originates from Ti atoms. A strong hybridization between Pt-, O- and Ti-states is also visible, between -6

eV and -2 eV for the approximant UTO, and between -7 eV and -3 eV for the complex hexagonal UTO. Using a smearing of the k-points set to the tetrahedron method with Blöchl corrections, a sharp pseudogap appears in the DOS of the hexagonal approximant (see inset in Fig.11(b) . Unfortunately, memory limitations did not allow a similar calculation to be performed with the square UTO.

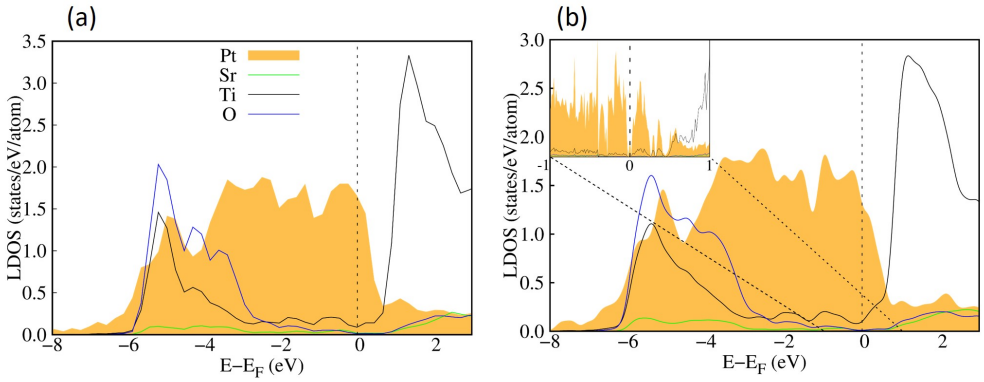

Figure 11: Density of states of the square approximant (a) and of the complex hexagonal phase (b). The inset in (b) shows the DOS calculated using a thinner k-point grid (2×2×1) exhibiting a sharp pseudogap at the Fermi energy.

Conclusion

In summary, we reported an all thin film approach to investigate ABO_3/Me(111) systems in a more versatile and less expensive way than by using single crystal metal substrates. The multilayer stacking consisted in a $SrTiO_3$ thin film deposited by PLD on a Pt(111) buffer epitaxialy grown on Al_2O_3(0001) substrate by MBE. The epitaxial relationships at both the Pt/Al_2O_3 and Pt/$SrTiO_3$ interfaces have been characterized by a combination of RHEED, XRD and HRTEM. Two novel UTO phases have been discovered in the wetting layer obtained by high temperature annealing of the thin film stacking: a square like approximant with a giant unit cell and a complex hexagonal phase. Their structures have been investigated by STM, LEED and DFT. High resolution STM images of both phases show bright protrusions located at the node of two different tilings constructed with the same basic square, triangle and 30° rhombus tiles possessing a common edge length of

about 6.7 Å. The tile ratio is different for the two phases. The number of tiles needed to describe the square approximant is twice as large as for the previously reported oblique approximant in the $SrTiO_3$/Pt(111) system. Using the experimentally derived tilings for these two new phases, structure models have been elaborated by adopting the tile decoration proposed by Cockayne *et al.*,[15] in which the Sr atoms are located at the node of the tiling and in which each Ti atom is bound to three oxygen atoms and each oxygen atom is located between two Ti atoms. Thus, the chemical compositions of the triangles, squares and rhombuses are $SrTiO_3$, $SrTi_4O_4$ and $SrTi_2O_2$, respectively, and the global compositions of the square and hexagonal phases are $Sr_{0.36}TiO_{1.54}$ and $Sr_{0.38}TiO_{1.56}$ respectively. Both phases have similar atom densities, formation enthalpies and adhesion energies. Both undergo significant structural relaxation when supported on Pt(111) leading to some buckling of the oxide layer. Charge transfer occurs from most electropositive elements (Sr, Ti) to most electronegative elements (Pt and O). According to the structural optimization, Ti cations lie more closely to the negatively charged Pt substrate compared to O and Sr atoms. Simulated STM images are found in excellent agreement with the experimental ones, thus giving support to the structural models proposed for the two new 2D oxide phases. Accordingly, mainly the Sr atoms are imaged by STM as they are protruding above the mean surface plane of the UTO thin films, although the main contribution to the DOS originates from Ti atoms. Finally, the DOS calculations suggest that the two new UTOs may have different physical and chemical properties. In perspective of this work, the all-thin-film approach proposed here may be expanded in the future to different families of ABO_3/Me(111) systems in order to explore the vast landscape offered by the numerous potential perovskites and metal supports for the discovery of new UTO 2D materials.

Data availability statement

The data that support the findings of this study are available upon reasonable request from the authors.

Conflict of interest statement

There are no conflicts to declare.

Acknowledgement

T.T.D. acknowledges the French PIA project "Lorraine Université d'Excellence" (ANR-15-IDEX-04-LUE) for financial support. S.S.P. and S.S acknowledge financial support by Slovenian Research Agency (P2-0084).This work is supported by the European Integrated Center for the Development of New Metallic Alloys and Compounds. E.G. and F.B. acknowledge financial support through the COMETE project (COnception in silico de Matériaux pour l'EnvironnemenT et l'Énergie) co-funded by the European Union under the program *F*EDER-FSE Lorraine et Massif des Vosges 2014-2020. This work was granted access to the HPC resources of TGCC, CINES and IDRIS under the allocation 99642 attributed by GENCI (Grand Equipement National de Calcul Intensif). High Performance Computing resources were also partially provided by the EXPLOR center hosted by the University de Lorraine (project 2017M4XXX0108).

Supporting Information Available

References

(1) J. B. Goodenough, Electronic and ionic transport properties and other physical aspects of perovskites, *Rep. Prog. Phys.*, 2004, **67**, 1915–1993 .

(2) D. G. Schlom, L. Chen, X. Pan, A. Schmehl, M. A. Zurbuchen, A thin film approach to engineering functionality into oxides. *J. Am. Ceram. Soc.*, 2008, **91**, 2429–2454 .

(3) J. Ngai, F. Walker, C. Ahn, Correlated Oxide Physics and Electronics. *Annu. Rev. Mater. Res.*, 2014, **44**, 1–17 .

(4) A. F.Santander-Syro, et al. Two-dimensional electron gas with universal subbands at the surface of SrTiO3. *Nature*, 2011, **469**, 189–193 .

(5) G. Barcaro, A. Fortunelli, 2D oxides on metal materials: concepts, status, and perspectives. *Phys. Chem. Chem. Phys.*, 2019, **21**, 11510–11536 .

(6) S. Förster, W. Widdra, in *Oxide Materials at the Two-Dimensional Limit*, ed. F. P. Netzer and A. Fortunelli, Springer, Berlin Heidelberg, 2016 .

(7) S. Förster, K. Meinel, R. Hammer, M. Trautmann, W.Widdra, Quasicrystalline structure formation in a classical crystalline thin-film system. *Nature*, 2013, **502**, 215–218 .

(8) D. Shechtman, I. Blech, D. Gratias, J. W. Cahn, Metallic phase with long-range orientational order and no translational symmetry. *Phys. Rev. Lett.*, 1984, **53**, 1951–1953 .

(9) S. Förster, J.I. Flege, E.M. Zollner, F.O. Schumann, R. Hammer, A. Bayat, K.M. Schindler,J. Falta,W. Widdra, Growth and decay of a two-dimensional oxide quasicrystal: High-temperature in situ microscopy. *Annalen der Physik*, 2017, **529**, 1600250 .

(10) Gähler, F. Crystallography of dodecagonal quasicrystals, in *Quasicrystalline materials: Proceedings of the I.L.L. Workshop*, ed. C. Janot.World Scientific, Singapore, 1988, 272-284 .

(11) S. Schenk, S. Förster, K. Meinel, R. Hammer, B. Leibundgut, M. Paleschke, J. Pantzer, C. Dresler, F.O. Schumann, W. Widdra, Observation of a dodecagonal oxide quasicrystal and its complex approximant in the $SrTiO_3$/Pt(1 1 1) system. *J. of Phys.: Condens. Matter*, 2017, **29**, 134002 .

(12) S. Förster, M. Trautmann, S. Roy, W. Adeagbo, E. Zollner, R. Hammer, F. Schumann, K. Meinel, S. Nayak, K. Mohseni, W. Hergert, H. Meyerheim, W. Widdra, Observation and structure determination of an Oxide quasicrystal approximant. *Phys. Rev. Lett.*, 2016, **117**, 095501 .

(13) A. I. Goldman, R. R. Kelton, Quasicrystals and crystalline approximants. *Reviews of Modern Physics*, 1993, **65**, 213–230 .

(14) T. Trevizam-Dorini, F. Brix, C. Chatelier, A. Kokalj, E. Gaudry, Two-dimensional oxide quasicrystal approximants with tunable electronic and magnetic properties. *Nanoscale*, 2021, **13**, 10771 .

(15) E. Cockayne, M. Mihalkovič, C. L. Henley, Structure of periodic crystals and quasicrystals in ultrathin films of Ba-Ti-O. *Phys. Rev. B*, 2016, **93**, 020101 .

(16) S. Förster, et al., Quasicrystals and their approximants in 2D ternary oxides. *Phys. Status Solidi B*, 2020, **257**, 1900624 .

(17) J. Goniakowski, C. Noguera, L. Giordano, G. Pacchioni, Adsorption of metal adatoms on FeO (111) and MgO (111) monolayers: Effects of charge state of adsorbate on rumpling of supported oxide film. *Phys. Rev. B*, 2009, **80**, 125403 .

(18) S. Schmidt, D. O. Klenov, S. P. Keane, J. Lu, T. E. Mates, S. Stemmera, Atomic structure of (111) $SrTiO_3$/Pt interfaces. *App. Phys. Lett.*, 2006, **88**, 131914 .

(19) R. Kilaas, Optimal and near-optimal filters in high-resolution electron microscopy. *Journal of Microscopy*, 1998, **190**, 45 .

(20) I. Horcas, R. Fernández, J. M. Gómez-Rodríguez, J. Colchero, J. Gómez-Herrero, A. M. Baro, WSXM: A software for scanning probe microscopy and a tool for nanotechnology. *Rev. Sci. Instruments*, 2007, **78**, 013705 .

(21) G. Kresse, J. Hafner, Ab Initio Molecular Dynamics for Liquid Metals. *Phys. Rev. B*, 1993, **47**, 558–561 .

(22) G. Kresse, J. Furthmüller, Efficient iterative schemes for ab initio total-energy calculations using a plane-wave basis set. *Phys. Rev. B*, 1996, **54**, 11169 – 11186 .

(23) G. Kresse, J. Furthmüller, Efficiency of ab-initio total energy calculations for metals and semiconductors using a plane wave basis set. *Comput. Mater. Sci.*, 1996, **6**, 15–50 .

(24) A. H. Larsen, et al., The atomic simulation environment—a Python library for working with atoms. *J. of Phys.: Condens. Matter*, 2017, **29**, 273002 .

(25) P. E. Blöchl, Projector augmented-wave method. *Physical Review B*, 1994, **50**, 17953 .

(26) G. Kresse, D. Joubert, From ultrasoft pseudopotentials to the projector augmented-wave method. *Phys. Rev. B*, 1999, **59**, 1758–1775 .

(27) J. Klimes, D. R. Bowler, A. Michaelides, Chemical accuracy for the van der Waals density functional. *J. Phys.: Condens. Mat.*, 2010, **22**, 022201 .

(28) J. Klimes, D. R. Bowler, A. Michaelides, Van der Waals density functionals applied to solids. *Phys. Rev. B*, 2011, **83**, 195131 .

(29) S. L. Dudarev, G. A. Botton, S. Y. Savrasov, C. J. Humphreys, A. P. Sutton, Electron energy loss spectra and the structural stability of nickel oxide: an LSDA+U study. *Phys. Rev. B*, 1998, **57**, 1505 .

(30) J. Goniakowski, C. Noguera, Intrinsic Properties of Pure and Mixed Monolayer Oxides in the Honeycomb Structure: M2O3 and MM'O3 (M, M' = Ti, V, Cr, Fe). *J. Phys. Chem. C*, 2019, **123**, 7898–7910 .

(31) O. Köksal, S. Baidya, R. Pentcheva, Confinement-driven electronic and topological phases in corundum-derived 3d-oxide honeycomb lattices. *Phys. Rev. B*, 2018, **97**, 035126 .

(32) J. Goniakowski, C. Noguera, Properties of metal-supported oxide honeycomb monolayers: M2O3 and MM'O3 on Me(111) (M, M ' = Ti, V, Cr, Fe; Me = Ag, Au, Pt). *J. Phys. Chem. C*, **2020**, **124**, 8186–8197 .

(33) This software is provided by the Henkelman group (University of Texas) and it can be found at http://theory.cm.utexas.edu/bader .

(34) W. Tang, E. Sanville, G. A. Henkelman, A grid-based Bader analysis algorithm without lattice bias. *J. of Phys.: Condens. Matter*, 2009, **21**, 084204 .

(35) E. Sanville, S. D. Kenny, R. Smith, G. Henkelman, Improved grid-based algorithm for Bader charge allocation. *Journal of Computational Chemistry*, 2007, **28**, 899–908 .

(36) R. F. W. Bader, Atoms in molecules: a quantum theory. *Chemical Reviews*, 1991, **91**, 893 .

(37) G. Henkelman, A. Arnaldsson, H. Jónsson, A fast and robust algorithm for Bader decomposition of charge density. *Computational Materials Science*, 2006, **36**, 354–360 .

(38) J. Tersoff, D. Hamann, Theory and application for the scanning tunneling microscope. *Phys. Rev. Lett.*, 1983,**50**, 1998–2001 .

(39) J. Tersoff, D. Hamann, Theory of the scanning tunneling microscope. *Phys. Rev. B*, 1985, **31**, 805 .

(40) K. Momma, F. Izumi, VESTA 3 for three-dimensional visualization of crystal, volumetric and morphology data. *Journal of Applied Crystallography*, 2011, **44**, 1272–1276 .

(41) The experimental observation of the square-like approximant phase was reported in[42] and simultaneously at the ECMetAC Days online conference in december 2020[43,44]

(42) C. Ruano M., L. Pasquier, S. Andrieu, K. Dumesnil, J. Ledieu, O. Copie, V. Fournée, M. Sicot, Observation of an oxide quasicrystal approximant in the $SrTiO_3$/Pt(111)/Al_20_3(0001) system. *Proceeding of the Aperiodic Research Network, online workshop, September 2020*, 2020

(43) C. Ruano M., L. Pasquier, S. Andrieu, K. Dumesnil, J. Ledieu, O. Copie, V. Fournée, M. Sicot, New quasicrystal approximants in the $SrTiO_3$/Pt(111)/Al_20_3(0001) system. *Proceeding of the ECMetAC Days, online conference, December 2020*, 2020

(44) S. Schenk, O. Krahn, S. Förster, W. Widdra, Dodecagonal oxide quasicrystal approximant with 72 tiling elements. *Proceeding of the ECMetAC Days, online conference, December 2020*, 2020

(45) C. Wu, M. R. Castell, J. Goniakowski, C. Noguera, Stoichiometry engineering of ternary oxide ultrathin films: BaxTi2O3 on Au(111). *Phys. Rev. B*, 2015, **91**, 155424

(46) S. Schenk, O. Krahn, H. Meyerheim, M. De Boissieu, S. Förster, W. Widdra, Large unit cell approximant derived from $SrTiO_3$ on Pt(111). *Proceeding of the International Research Network "Open space between aperiodic order and physics and chemistry of materials", Carry le Rouet, October 2021*, 2021